Published by Avanti Publishers

Journal of Chemical Engineering Research Updates

ISSN (online): 2409-983X

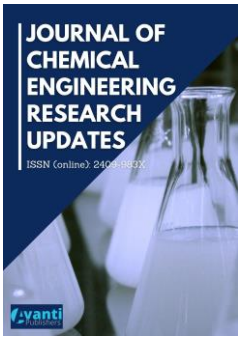

Zr-Doping-Induced Structural and Lattice-Oxygen Regulation in $CeZrO_x$ Solid Solutions for Chemical-Looping Oxidative Dehydrogenation of Propane

Tuo Guo, Dongling Zhao and Qingjie Guo*

Center of Carbon Capture and Industrial Utilization, Jiangmen Laboratory of Carbon Science and Technology, Jiangmen 529020, China

ARTICLE INFO

Article Type: Research Article

Academic Editor: Meng He

Keywords:
Redox cycle
Propylene synthesis
CeO_2-ZrO_2 solid solution
Lattice oxygen selectivity
Crystal facet engineering

Timeline:
Received: May 18, 2026
Accepted: July 07, 2026
Published: August 17, 2026

Citation: Guo T, Zhao D, Guo Q. Zr-doping-induced structural and lattice-oxygen regulation in $CeZrO_x$ solid solutions for chemical-looping oxidative dehydrogenation of propane. J Chem Eng Res Updates. 2026; 13: 19-31.

DOI: https://doi.org/10.15377/2409-983X.2026.13.2

ABSTRACT

Chemical-looping oxidative dehydrogenation of propane (CL-ODHP) separates hydrocarbon conversion from gas-phase oxygen and uses a redox-active solid as the oxygen source. Here, $Ce_{1-Y}Zr_YO_x$ (y = 0–0.50) oxygen carriers were prepared by co-precipitation to examine how moderate Zr doping changes fluorite-lattice structure, mesoporosity, oxygen speciation, and transient CL-ODHP performance at 550 °C under identical fixed-bed conditions using a 10% propane feed. X-ray diffraction showed progressive lattice contraction and a composition-dependent relative intensity of the (111) reflection, with $Ce_{0.90}Zr_{0.10}O_x$ giving the largest relative (111) intensity among the mixed oxides. This composition also exhibited the highest BET surface area (111.24 $m^2\ g^{-1}$), pore volume (0.36 $cm^3\ g^{-1}$), mean pore diameter (17.79 nm), and XPS lattice-oxygen fraction (O_I, 47.87%), while maintaining a lower defect-associated O_II fraction (28.37%) than the more Zr-rich samples. From the data points plotted over 3–15 min, $Ce_{0.90}Zr_{0.10}O_x$ provided the highest mean propane conversion (16.85%), propylene selectivity (63.57%), and propylene yield (10.71%) within the evaluated series. Its apparent oxygen-depletion/deactivation constant was 0.0113 min^{-1}, lower than those of CeO_2 (0.0258 min^{-1}) and $Ce_{0.95}Zr_{0.05}O_x$ (0.0144 min^{-1}). The novelty of this work is the within-series correlation of relative (111) diffraction intensity, mesoporous structure, and standardized O_I/O_II/O_III surface-oxygen components with transient propane conversion and selectivity, identifying moderate Zr substitution as a balance between accessible lattice oxygen and defect-associated oxygen. These results are consistent with, but do not by themselves prove, a Mars-van Krevelen pathway. Because the study comprises single-run reduction-half-cycle screening without independent replication or multicycle regeneration, the quantitative performance should be regarded as preliminary rather than a record benchmark.

*Corresponding Author
Email: qingjie_guo@vip.sina.com
Tel: +(86) 15192551136

1. Introduction

Propylene serves as a crucial foundational chemical building block and stands as the second-largest chemical feedstock globally, superseded only by ethylene [1]. Industrially, it is widely utilized for the synthesis of high-value-added derivatives, including polypropylene, acrylonitrile, and propylene oxide [2]. According to recent reports, the global demand for propylene currently reaches approximately 80 million metric tons annually [3]. Conventionally, the production of light olefins has predominantly relied on steam cracking (SC) and fluid catalytic cracking (FCC) [4]. Steam cracking typically employs feedstocks such as liquefied petroleum gas (LPG) and naphtha, utilizing homogeneous gas-phase reactions to thermally cleave hydrocarbons into lighter olefins [5]. Alternatively, FCC processes utilize heavier feedstocks, such as vacuum gas oil (VGO), refinery hydrocarbon residues, and deasphalted oil—upgrading them into lighter, more valuable products [6]. However, these traditional cracking reactions are highly endothermic, requiring massive energy inputs and necessitating operation within specialized high-temperature-resistant reactors. Moreover, these elevated temperatures inevitably provoke extensive coke formation, which imposes severe operational constraints on the process [7, 8].

Driven by the surging availability of shale gas, the demand for efficient pathways to upgrade low-cost propane into propylene, a foundational chemical feedstock has escalated. Conventional production methods, such as steam cracking and fluid catalytic cracking, are highly endothermic, energy-intensive, and prone to severe coke formation. Direct propane dehydrogenation (PDH) offers a targeted alternative, yet its equilibrium conversion is strictly thermodynamically limited. The requisite high operating temperatures exacerbate thermal cracking, inducing rapid catalyst deactivation via sintering and coking [9, 10]. While conventional oxidative dehydrogenation (ODH) bypasses these thermodynamic constraints exothermically, co-feeding gaseous O_2 triggers deep oxidation into CO_x, severely suppressing propylene selectivity and necessitating capital-intensive air separation units [11].

Chemical looping oxidative dehydrogenation (CL-ODH) emerges as a robust paradigm to overcome these fundamental limitations by employing a solid oxygen carrier in a decoupled redox cycle [12]. In the primary reactor, propane is selectively oxidized by the oxygen carriers' lattice oxygen; the *in-situ* generation and condensation of water shift the thermodynamic equilibrium toward the products, significantly enhancing propylene yield. The reduced oxygen carrier is subsequently regenerated with ambient air in a secondary reactor [13, 14]. By preventing direct contact between propane and gaseous O_2, CL-ODH intrinsically mitigates explosion hazards and suppresses deep oxidation. Furthermore, it completely eliminates the need for expensive air separation infrastructure. Coupled with the robust redox cycling stability of modern oxygen carriers, CL-ODH presents a highly viable, cost-effective, and safe strategy for industrial-scale propylene synthesis [15, 16].

Among oxygen-carrier candidates, CeO_2 is attractive because of its oxygen-storage capacity and redox kinetics commonly discussed within a Mars–van Krevelen framework [17]. Pure ceria can nevertheless present surface oxygen environments that favor non-selective deep oxidation of propane or propylene to CO_x. Incorporating smaller Zr^{4+} ions into the CeO_2 fluorite lattice is an established approach to contract/distort the lattice and modify oxygen-defect formation and mobility [18-20]. These changes may improve C–H activation, but excessive defect-associated oxygen can also intensify non-selective oxidation; an optimum composition must therefore balance oxygen accessibility and selectivity.

Despite the proven advantages of Zr doping in modulating bulk lattice oxygen mobility, a profound understanding of the intrinsic mapping between specific surface atomic arrangements (i.e., exposed crystal facets) and macroscopic catalytic selectivity remains scarce. In heterogeneous catalytic oxidation, the CeO_2 system exhibits pronounced structure-sensitivity. Xie *et al*. explicitly highlighted that in propane ODH over CeO_2, the reaction pathways are heavily dictated by the specific exposed facets (e.g., {110}, {100}, or {111}), resulting in distinct C–H bond activation pathways and product desorption energy barriers [21]. At the microscopic level, the geometric configuration of these facets directly dictates the formation energy of oxygen vacancies and the synergistic catalytic effects at the gas-solid interface. For instance, studies by Zhang *et al*. and Zhou *et al*. indicate that specific morphologies and exposed facets, particularly the (111) facet, which possesses the lowest surface energy and highest atomic packing density, not only precisely regulate the local oxygen defect density but also

profoundly influence the lattice oxygen replenishment cycle and the adsorption-desorption kinetics of reactants [22, 23].

Accordingly, this study evaluates a $Ce_{1-y}Zr_yO_x$ series under identical transient CL-ODHP conditions to test how Zr substitution changes the fluorite lattice, relative (111) diffraction intensity, mesoporous texture, and surface oxygen components. The intended contribution is a composition-resolved structure–oxygen-speciation–performance correlation rather than a claim of record catalytic performance. In particular, we examine whether moderate Zr incorporation can retain a high lattice-oxygen fraction while avoiding the larger defect-associated oxygen fraction observed at high Zr content, and whether this balance corresponds to improved propane conversion and propylene selectivity.

2. Materials and Methods

2.1. Preparation of $Ce_{1-y}Zr_yO_x$ Oxygen Carriers

The $Ce_{1-y}Zr_yO_x$ (y = 0.05, 0.10, 0.25, and 0.50) oxygen carriers were prepared by co-precipitation. $Ce(NO_3)_3{\cdot}6H_2O$ and the reported zirconium nitrate precursor were dissolved in deionized water in the required stoichiometric ratio. After complete dissolution, 1 mol L^{-1} Na_2CO_3 was added dropwise until pH 7. The suspension was stirred in a 70 °C oil bath for 4 h and aged for 2 h. The solid was recovered by vacuum filtration, washed alternately with water and ethanol three times, dried at 90 °C for 12 h, and calcined at 600 °C for 4 h using a heating rate of 3 °C min^{-1}. After cooling, the samples were ground and sieved.

2.2. CL-ODHP Performance Test

The oxygen-carrier performance was evaluated in a fixed-bed quartz reactor (Fig. **1**). A 0.5 g sample was placed in the isothermal zone and heated from room temperature to 550 °C at 10 °C min^{-1} under N_2. After a 20 min N_2 purge, a feed containing 45 mL min^{-1} N_2 and 5 mL min^{-1} C_3H_8 was introduced. The total flow of 50 mL min^{-1} (3.0 L h^{-1}) and the reported GHSV of 1440 h^{-1} correspond to a nominal bed volume of 2.08 mL. This GHSV was held constant as a comparative screening condition; because no GHSV-independence or particle-size test was performed, kinetic-control and absence of transport limitations are not claimed. Effluent was collected over successive 3 min intervals and analyzed by gas chromatography (A91 Plus, Panna). Each composition was evaluated in one screening run under identical conditions; no independent replicate set was available for calculating standard deviations. Accordingly, Figs. 9–11 show single-run apparent values without error bars, which is a limitation of the present study.

Propane conversion, propylene selectivity, CO_x selectivity, and propylene yield were calculated by carbon-normalized product analysis as follows:

$$X_{C_3H_8}=\frac{N_{C_3H_6}+\frac{2}{3}N_{C_2}+\frac{1}{3}N_{C_1}}{N_{C_3}+\frac{2}{3}N_{C_2}+\frac{1}{3}N_{C_1}}\times 100\% \quad \text{Eq. (1)}$$

$$S_{C_3H_6}=\frac{N_{C_3H_6}}{N_{C_3H_6}+\frac{2}{3}N_{C_2}+\frac{1}{3}N_{C_1}}\times 100\% \quad \text{Eq. (2)}$$

$$S_{CO_X}=\frac{N_{CO_X}}{N_{C_3H_6}+\frac{2}{3}N_{C_2}+\frac{1}{3}N_{C_1}}\times 100 \quad \text{Eq. (3)}$$

$$Y_{C_3H_6}=X_{C_3H_8}\times S_{C_3H_6} \quad \text{Eq. (4)}$$

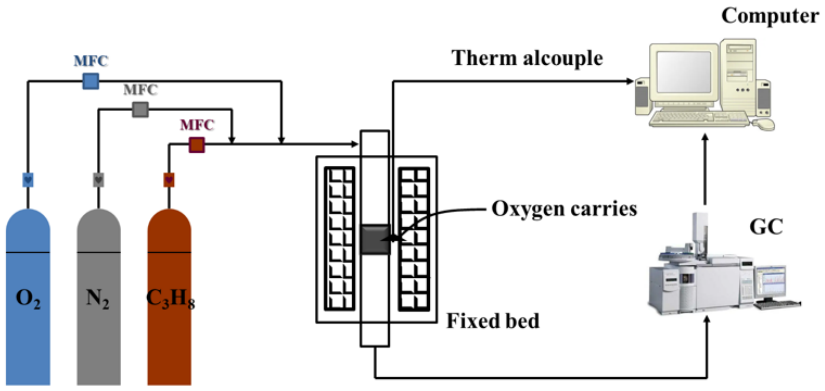

Figure 1: Fixed-bed reactor used for propane CL-ODH.

2.3. Characterization Methods

The crystal structure of the oxygen carriers was identified by powder X-ray diffraction (XRD) using a Rigaku Ultima IV instrument. The specific surface area, pore volume, and pore diameter of the oxygen carriers were determined using an ASAP 2010 analyzer. The micromorphology of the oxygen carrier samples was characterized by a JSMS-6700F series scanning electron microscope (SEM). An FEI Talos F200S field emission electron microscope (TEM) was employed to observe the microstructure of the oxygen carriers. Raman spectra were recorded using a Horiba Raman spectrometer (iHR320) equipped with a CCD detector. Hydrogen temperature-programmed reduction (H_2-TPR) was performed on an Auto Chemiln 2960 chemisorption analyzer manufactured by Quantachrome Instruments. The elemental valence states of the oxygen carriers were characterized by X-ray photoelectron spectroscopy (XPS) using an ESCAL 250xi photoelectron spectrometer produced by an American company.

3. Results and Discussion

3.1. Physicochemical Characterization

The XRD patterns of the $CeZrO_x$ mixed-oxide oxygen carriers are presented in Fig. (**2**). For CeO_2, reflections at 2θ = 28.52°, 33.03°, 47.46°, and 56.41° were assigned to the (111), (200), (220), and (311) planes of cubic fluorite CeO_2, respectively [24]. With Zr doping, the (111) reflection shifted to higher 2θ, consistent with lattice contraction caused by substitution of smaller Zr^{4+} for Ce^{4+} [25]. The 28–30° inset in Fig. (**2**) magnifies this shift. The calculated lattice parameters are listed in Table **1**; the unit-cell volume decreased from 158.46 Å³ for CeO_2 to 139.58 Å³ for

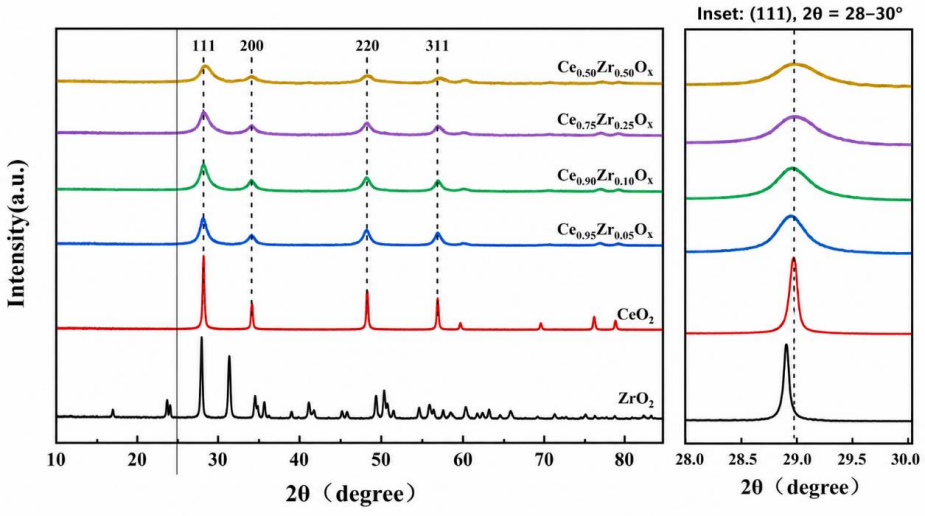

Figure 2: XRD patterns of fresh ZrO_2, CeO_2, and $CeZrO_x$ oxygen carriers; inset: enlarged (111) region at 2θ = 28–30°.

$Ce_{0.50}Zr_{0.50}O_x$. XRD relative intensities are used here as a composition-dependent structural descriptor and are not treated as a direct quantitative measurement of exposed surface-facet area.

Because the reaction occurs at the gas–solid interface, the composition-dependent diffraction intensities were compared using the relative intensities of the (111), (200), (220), and (311) reflections (Table **S1**). The relative (111) intensity varied more strongly than the other reflections and was largest for $Ce_{0.90}Zr_{0.10}O_x$; the sequence was $Ce_{0.90}Zr_{0.10}O_x$ > $Ce_{0.75}Zr_{0.25}O_x$ > $Ce_{0.95}Zr_{0.05}O_x$ > $Ce_{0.50}Zr_{0.50}O_x$. This correlation is discussed alongside texture and oxygen speciation, without assigning causality to the diffraction intensity alone.

Table 1: Crystallite size and lattice parameters of CeO_2 and $CeZrO_x$ mixed-oxide oxygen carriers.

Oxygen Carrier	Crystallite Size (Å)	Lattice Parameter (Å)	Unit-cell Volume (Å³)
CeO_2	180.37	5.78	158.46
$Ce_{0.95}Zr_{0.05}O_x$	171.24	5.72	157.21
$Ce_{0.90}Zr_{0.10}O_x$	152.66	5.63	150.68
$Ce_{0.75}Zr_{0.25}O_x$	160.05	5.58	146.34
$Ce_{0.50}Zr_{0.50}O_x$	168.94	5.32	139.58

Fig. (**3**) and Table **2** summarize N_2 adsorption–desorption behavior. The curves are Type IV isotherms with H3 hysteresis loops, which is consistent with mesoporous aggregates containing slit-like interparticle pores [26]. On adding Zr, the BET surface area, pore volume, and mean pore diameter first increased and then decreased, reaching 111.24 $m^2\ g^{-1}$, 0.36 $cm^3\ g^{-1}$, and 17.79 nm, respectively, for $Ce_{0.90}Zr_{0.10}O_x$. The larger pores may facilitate molecular transport and propylene desorption [27], although transport measurements were not performed.

Table 2: Pore-structure parameters of the oxygen carriers.

Samples	S_{BET} (m^2/g)[a]	V_p (cm^3/g)[b]	D_p (nm)[c]
CeO_2	70.46	0.23	12.13
$Ce_{0.95}Zr_{0.05}O_X$	103.09	0.28	15.46
$Ce_{0.90}Zr_{0.10}O_X$	111.24	0.36	17.79
$Ce_{0.75}Zr_{0.25}O_X$	93.77	0.31	14.31
$Ce_{0.50}Zr_{0.50}O_X$	78.36	0.25	11.88
ZrO_2	54.58	0.14	8.33

a: Calculated using the BET equation; **b:** Single-point pore volume calculated from the adsorption isotherm at P/P_0 = 0.99.
c: Average pore diameter calculated by applying the BJH method to the desorption isotherm.

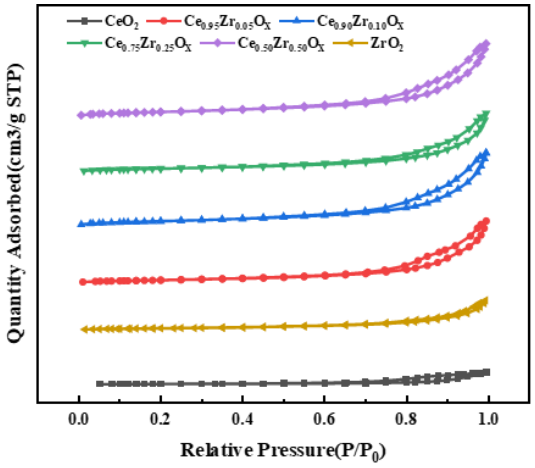

Figure 3: N_2 adsorption–desorption isotherms (Type IV with H3 hysteresis loops) of the oxygen carriers.

SEM images of the CeO_2 and $CeZrO_x$ carriers are shown in Fig. (**4**). CeO_2 exhibits a rod-like morphology, whereas the Zr-containing mixed oxides form disordered particulate aggregates. $Ce_{0.90}Zr_{0.10}O_x$ shows visible interparticle voids, while $Ce_{0.75}Zr_{0.25}O_x$ and $Ce_{0.50}Zr_{0.50}O_x$ appear more densely aggregated. These qualitative observations are consistent with the composition-dependent porosity in Table **2**, but do not by themselves establish gas-diffusion coefficients.

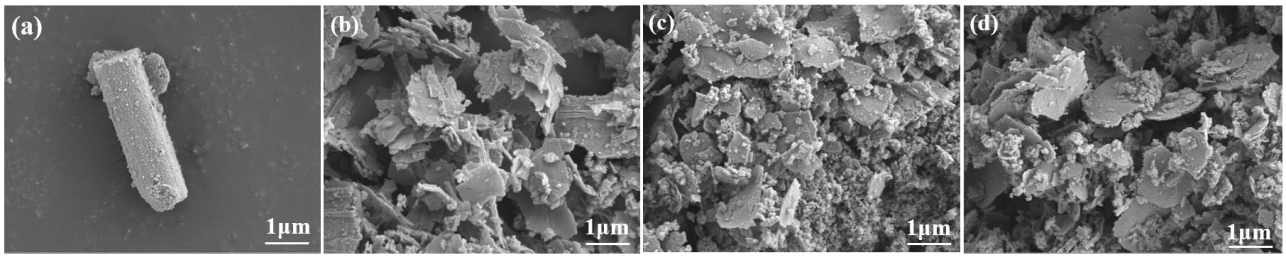

Figure 4: SEM images of (a) CeO_2, (b) $Ce_{0.90}Zr_{0.10}O_x$, (c) $Ce_{0.75}Zr_{0.25}O_x$, and (d) $Ce_{0.50}Zr_{0.50}O_x$ oxygen carriers. Scale bars = 1 μm in all panels.

Fig. (**5**) displays the TEM images of the $Ce_{0.90}Zr_{0.10}O_x$ oxygen carrier, further corroborating the cubic fluorite structure of the CeO_2 matrix. The polycrystalline material comprises small, randomly oriented crystalline domains. The observed lattice fringe spacings of d = 0.31 nm, 0.26 nm, 0.19 nm, and 0.16 nm correspond precisely to the (111), (200), (220), and (311) facets, respectively, verifying the successful synthesis of the target structural configurations.

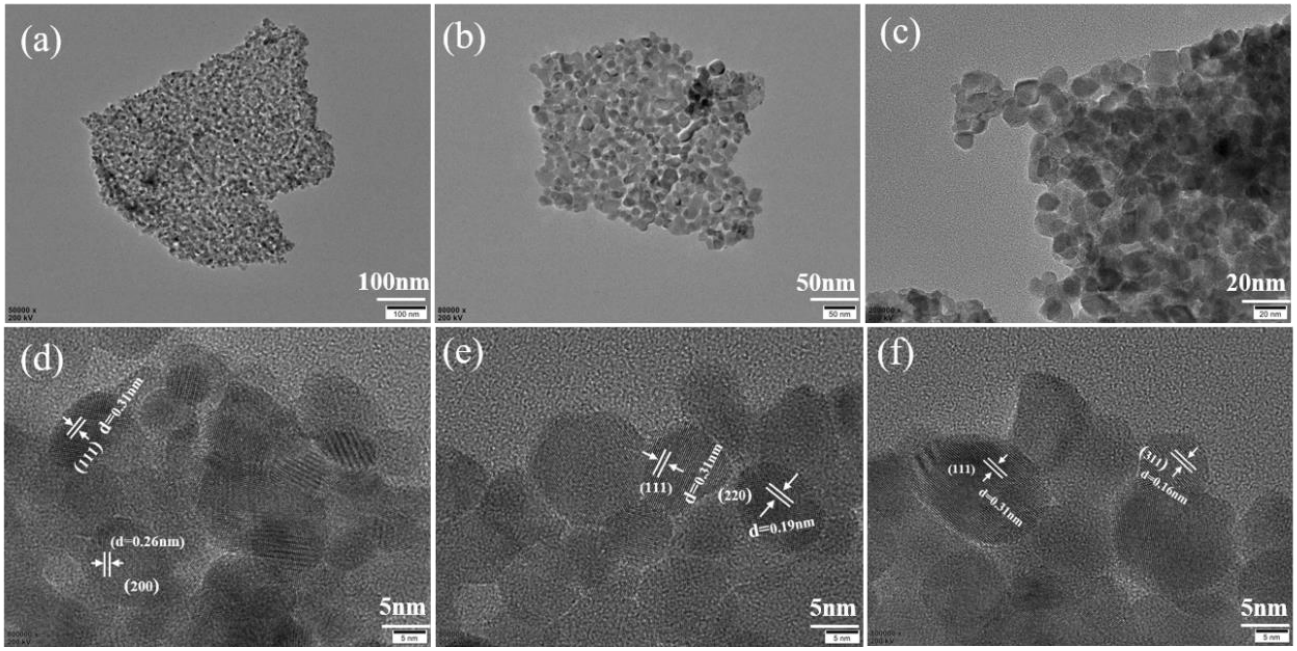

Figure 5: TEM and high-resolution TEM images of the $Ce_{0.90}Zr_{0.10}O_x$ oxygen carrier.

Fig. (**6**) shows the O 1s XPS spectra. To avoid ambiguous terminology, three fitted components are used consistently: O_I, lattice oxygen (527.91–528.17 eV); O_II, a defect-associated/oxygen-vacancy-related component (529.36–529.87 eV); and O_III, hydroxyl and surface-adsorbed oxygen (531.15–531.51 eV) [28]. O_II is an operational XPS assignment rather than a direct count of crystallographic vacancies. Table **3** reports all three fractions. $Ce_{0.90}Zr_{0.10}O_x$ had the largest O_I fraction (47.87%), whereas $Ce_{0.50}Zr_{0.50}O_x$ had the largest O_II fraction (38.65%). Defect formation can increase lattice-oxygen mobility, but an excessive defect-associated component may also promote non-selective oxidation [29-31]. The fitted component curves are shown in Fig. (**6**); a residual trace cannot be reconstructed from the embedded image and should be exported from the original fitting project if the raw XPS fit files are available.

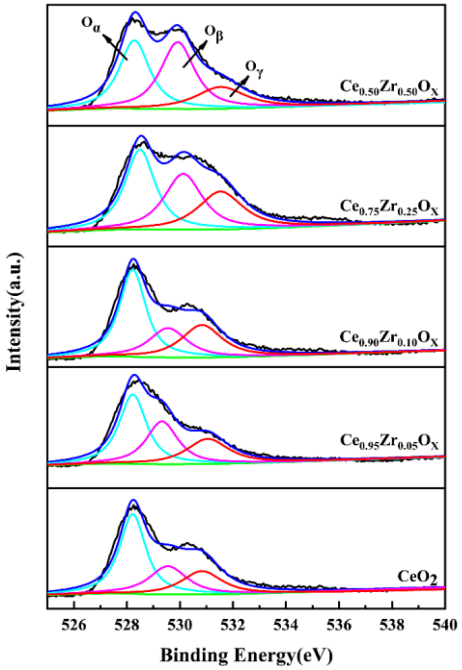

Figure 6: O 1s XPS spectra and fitted O_I (lattice oxygen), O_II (defect-associated/oxygen-vacancy-related), and O_III (hydroxyl/surface-adsorbed oxygen) components of CeO_2 and $CeZrO_x$ oxygen carriers.

Table 3: Relative Ce valence and O 1s component fractions of CeO_2 and $CeZrO_x$ oxygen carriers.

Oxygen Carrier	$Ce^{3+}/(Ce^{3+}+Ce^{4+})$ (%)	O_I (%)	O_II (%)	O_III (%)
CeO_2	22.06	43.34	27.07	29.59
$Ce_{0.95}Zr_{0.05}O_X$	26.09	41.85	31.33	26.82
$Ce_{0.90}Zr_{0.10}O_X$	24.37	47.87	28.37	23.76
$Ce_{0.75}Zr_{0.25}O_X$	29.96	39.10	36.14	24.76
$Ce_{0.50}Zr_{0.50}O_X$	34.58	36.44	38.65	24.91

The dominant Raman band at approximately 463 cm^{-1} is assigned to the F_2g mode of fluorite CeO_2 [32]. Its shift with Zr loading supports solid-solution formation [33]. Peak broadening can arise from both finite crystallite size and lattice disorder; therefore, FWHM should not be interpreted as a vacancy measure in isolation [34, 35]. Comparison with Table **1** decouples these effects qualitatively: $Ce_{0.90}Zr_{0.10}O_x$ has a smaller XRD crystallite size (152.66 Å) than $Ce_{0.50}Zr_{0.50}O_x$ (168.94 Å), yet its F_2g FWHM is narrower (30.23 versus 36.03 cm^{-1}) (Table **4**). Thus, crystallite size alone cannot explain the broadest band. The larger O_II fraction of $Ce_{0.50}Zr_{0.50}O_x$ (38.65% versus 28.37% for $Ce_{0.90}Zr_{0.10}O_x$) indicates that defect-related disorder is the dominant additional contribution within this comparison (Fig. **7**).

Table 4: Raman F_2g full width at half maximum (FWHM) of CeO_2 and $CeZrO_x$ oxygen carriers.

Oxygen Carrier	Raman FWHM/cm^{-1}
CeO_2	26.48
$Ce_{0.95}Zr_{0.05}O_x$	33.17
$Ce_{0.90}Z_{r0.10}O_x$	30.23
$Ce_{0.75}Zr_{0.25}O_x$	31.86
$Ce_{0.50}Zr_{0.50}O_x$	36.03

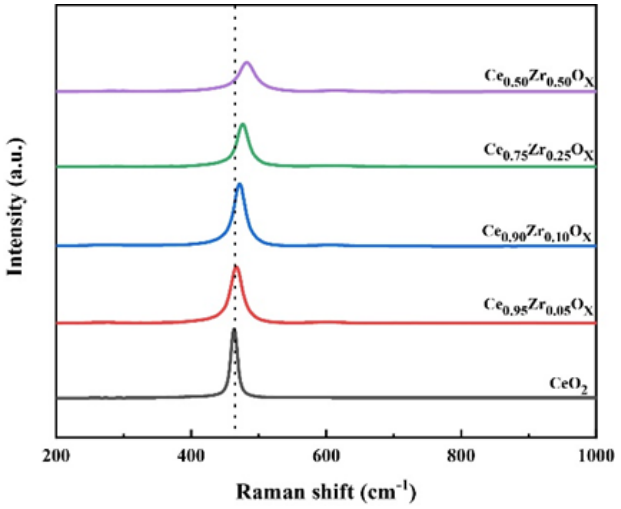

Figure 7: Raman spectra of CeO_2 and $CeZrO_x$ oxygen carriers.

The H_2-TPR profiles are shown in Fig. (**8**). No separate Zr^{4+} reduction peak was observed below 1000 °C [36]. The low-temperature feature at approximately 510–541 °C is assigned primarily to reduction of surface-accessible Ce^{4+}, whereas the higher-temperature feature near 730 °C is assigned to bulk CeO_2 reduction [37]. The feature near 550 °C is therefore not assigned simultaneously to both surface and bulk processes. At higher Zr contents, overlap between broad contributions cannot be excluded; quantitative separation would require the original TPR signal and baseline. Because those raw files were not available in the submitted document, no numerical deconvolution has been introduced. The reported increase in H_2 consumption from 62.81 to 106.77 μmol g^{-1} is interpreted as increased reducible-oxygen capacity, while XPS and Raman provide complementary evidence of defect formation [38].

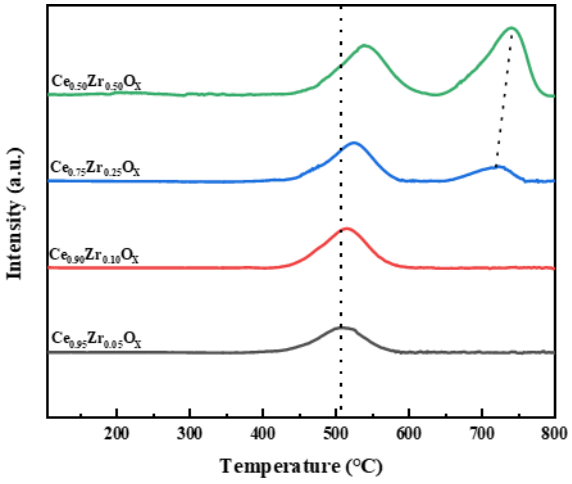

Figure 8: H_2-TPR profiles of $CeZrO_x$ oxygen carriers.

3.2. Effect of Oxygen-Carrier Composition on Propane Conversion

Fig. (**9**) shows the temporal evolution of propane conversion. The plotted data decrease as the finite lattice-oxygen inventory is consumed. Values recalculated from the plotted points over 3–15 min give mean conversions of 11.02% (CeO_2), 16.85% ($Ce_{0.90}Zr_{0.10}O_x$), 9.33% ($Ce_{0.75}Zr_{0.25}O_x$), 13.60% ($Ce_{0.95}Zr_{0.05}O_x$), 7.27% ($Ce_{0.50}Zr_{0.50}O_x$), and 5.39% (ZrO_2). A post hoc pseudo-first-order fit, $X(t) = X_0 \exp(-k\_d\ t)$, to the five plotted points from 3 to 15 min gave apparent oxygen-depletion/deactivation constants of 0.0258 min^{-1} (CeO_2, $R^2 = 0.983$), 0.0144 min^{-1} ($Ce_{0.95}Zr_{0.05}O_x$, $R^2 = 0.954$), 0.0113 min^{-1} ($Ce_{0.90}Zr_{0.10}O_x$, $R^2 = 0.933$), 0.0105 min^{-1} ($Ce_{0.75}Zr_{0.25}O_x$, $R^2 = 0.916$), 0.0125 min^{-1} ($Ce_{0.50}Zr_{0.50}O_x$, $R^2 = 0.978$), and 0.0162 min^{-1} (ZrO_2, $R^2 = 0.967$). $Ce_{0.90}Zr_{0.10}O_x$ therefore combined the highest

initial/mean conversion with slower decay than CeO_2 and $Ce_{0.95}Zr_{0.05}O_x$, although $Ce_{0.75}Zr_{0.25}O_x$ had a slightly smaller fitted k_d. These apparent constants describe the transient plotted response and are not intrinsic kinetic constants.

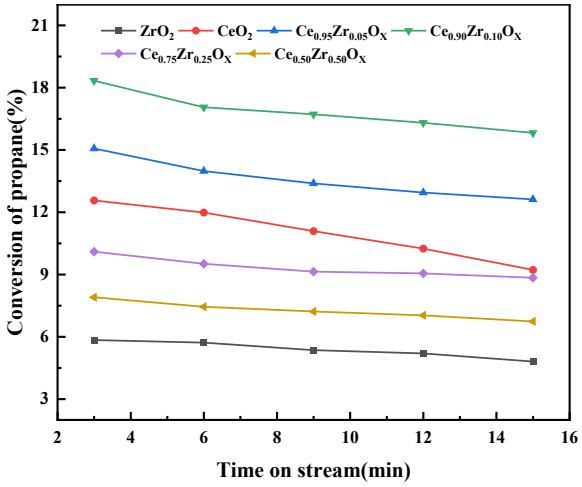

Figure 9: Effect of CeO_2, ZrO_2, and $CeZrO_x$ oxygen carriers on propane conversion at 550 °C. Single-run values; no independent-replicate error bars are available.

3.3. Effect of Oxygen-Carrier Composition on Propylene Selectivity

Fig. (**10**) summarizes propylene selectivity. Values recalculated from the plotted points over 3–15 min give mean selectivities of 50.87% (CeO_2), 63.57% ($Ce_{0.90}Zr_{0.10}O_x$), 53.69% ($Ce_{0.75}Zr_{0.25}O_x$), 57.57% ($Ce_{0.95}Zr_{0.05}O_x$), 45.87% ($Ce_{0.50}Zr_{0.50}O_x$), and 35.51% (ZrO_2). The high mean selectivity of $Ce_{0.90}Zr_{0.10}O_x$ coincides with its larger pores, highest O_I fraction, and moderate O_II fraction. By contrast, $Ce_{0.50}Zr_{0.50}O_x$ combines a larger O_II fraction with lower selectivity, consistent with more non-selective oxidation. The data support a parallel network in which propane can form propylene or $C_1/C_2/CO_x$ products, together with possible sequential propylene oxidation to CO_x. Because selectivity varies less strongly with time than conversion, primary branching from adsorbed propane is likely important; however, product-specific transient experiments are required to quantify the sequential route.

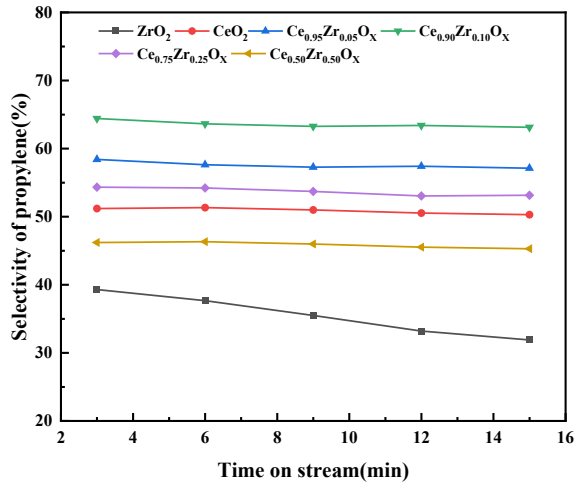

Figure 10: Effect of CeO_2, ZrO_2, and $CeZrO_x$ oxygen carriers on propylene selectivity at 550 °C. Single-run values; no independent-replicate error bars are available.

3.4. Effect of Oxygen-Carrier Composition on Propylene Yield

Fig. (**11**) shows the transient propylene yield. Values recalculated from the plotted points over 3–15 min give mean yields of 5.61% (CeO_2), 10.71% ($Ce_{0.90}Zr_{0.10}O_x$), 5.01% ($Ce_{0.75}Zr_{0.25}O_x$), 7.83% ($Ce_{0.95}Zr_{0.05}O_x$), 3.34%

($Ce_{0.50}Zr_{0.50}O_x$), and 1.92% (ZrO_2). $Ce_{0.90}Zr_{0.10}O_x$ therefore gave the highest mean yield within the tested series. This within-series result should not be interpreted as a record benchmark because no literature-normalized productivity comparison, independent replication, or multicycle test was performed.

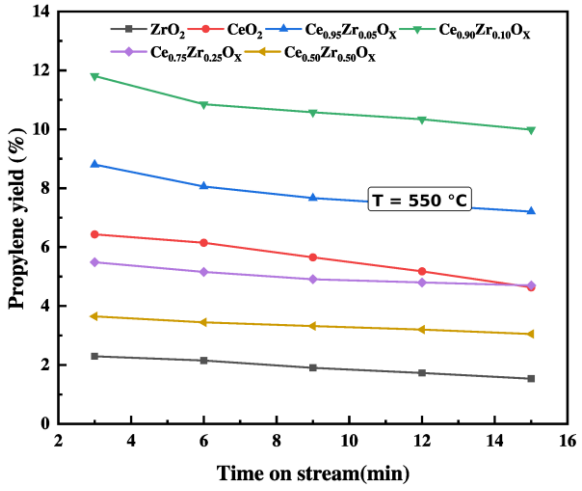

Figure 11: Effect of CeO_2, ZrO_2, and $CeZrO_x$ oxygen carriers on propylene yield at 550 °C. Single-run values; no independent-replicate error bars are available.

3.5. Mechanistic, Thermodynamic, and Engineering Implications

The combined XPS, Raman, and H_2-TPR results are consistent with a proposed Mars–van Krevelen sequence on $Ce_{0.90}Zr_{0.10}O_x$: (i) C_3H_8 adsorption on the $CeZrO_x$ surface, including regions associated with the fluorite (111) structure; (ii) C–H activation by O_I lattice oxygen and formation of C_3H_6 and H_2O; (iii) desorption of C_3H_6 and H_2O, leaving a vacancy/defect site; and (iv) restoration of lattice oxygen during a separate air-regeneration step. In shorthand: $C_3H_8(g) \rightarrow C_3H_8^* \rightarrow C_3H_6(g) + H_2O(g) + V\_O$; $V\_O + 1/2\ O_2 \rightarrow O\_latt$. The measured O_I/O_II balance and reducibility support oxygen availability and mobility, but they do not directly observe elementary steps or demonstrate regeneration, so the mechanism remains a working hypothesis.

An illustrative ideal-gas equilibrium calculation was made for direct PDH, $C_3H_8 \rightleftharpoons C_3H_6 + H_2$, using NIST gas-phase thermochemical data [40]. At 550 °C, K_p is approximately 0.106; for a 10 mol% propane/90 mol% N_2 feed at 1 bar, this corresponds to an equilibrium propane conversion of approximately 64% (approximately 31% for an undiluted 1 bar propane feed). The observed mean conversion of 16.85% is below, not above, this direct-PDH equilibrium value. The advantage of CL-ODH in the present context is therefore the alternative lattice-oxygen redox pathway, physical separation from gaseous O_2, and potential heat integration, rather than demonstrated equilibrium exceedance [41-43]. ODH can reduce external heat duty relative to strongly endothermic PDH, and heat from carrier reoxidation may be integrated with the reduction reactor [15, 43]; however, no process simulation, energy balance, or exergy analysis was performed here, so a numerical energy-saving claim would be premature.

Recent chemical-looping studies have used promoted redox phases, dual-functional mixed oxides, and engineered interfaces to increase olefin selectivity and cyclic stability [44-50]. Relative to those catalyst-integrated or interface-engineered systems, the present unpromoted $CeZrO_x$ series shows modest performance. Its narrower novelty is the internally consistent comparison linking Zr content, relative (111) diffraction intensity, mesoporosity, and O_I/O_II/O_III fractions under one set of transient conditions. A separate catalyst is not mechanistically mandatory because a redox-active oxygen carrier can itself provide reaction sites [42, 43], but catalyst–carrier coupling may improve performance. The present work is limited to the propane-contact half-cycle; air regeneration, multicycle stability, carbon balance closure, GHSV/particle-size independence, independent replication, and bifunctional catalyst coupling remain necessary future work.

4. Conclusions

$Ce_{1-Y}Zr_YO_x$ mixed oxides retained the cubic fluorite structure while Zr substitution contracted the lattice and modified mesoporosity and surface oxygen speciation. Within the tested series, $Ce_{0.90}Zr_{0.10}O_x$ showed the largest relative (111) diffraction intensity, highest BET surface area (111.24 $m^2\ g^{-1}$), largest mean pore diameter (17.79 nm), highest O_I lattice-oxygen fraction (47.87%), and a moderate O_II defect-associated fraction (28.37%). From the plotted single-run data at 550 °C, this composition gave the highest mean propane conversion (16.85%), propylene selectivity (63.57%), and propylene yield (10.71%), with an apparent oxygen-depletion/deactivation constant of 0.0113 min^{-1}. Comparison of Raman FWHM with XRD crystallite size indicates that defect-related disorder, rather than size alone, makes an important contribution to band broadening. The correlations are consistent with a Mars–van Krevelen-type use of lattice oxygen, but they do not establish elementary steps or cyclic regeneration. Thus, moderate Zr substitution provides a useful composition-level balance between accessible lattice oxygen and defect-associated oxygen; independent replication, mass-transfer tests, complete carbon balances, multicycle regeneration, and catalyst–carrier coupling are required before industrial or record-performance claims can be made.

Conflict of Interest

The authors declare that they have no known competing financial interests or personal relationships that could have appeared to influence the work reported in this paper.

Funding

The authors are very grateful to the Open Research Fund of State Key Laboratory of Mesoscience and Engineering (No. MESO-25-D02).

Data Availability

The data reported in this study are contained in the manuscript and Supporting Information.

References

[1] Phung TK, Pham TLM, Vu KB, Busca G. (Bio)Propylene production processes: A critical review. J Environ Chem Eng. 2021; 9(4): 105673. https://doi.org/10.1016/j.jece.2021.105673

[2] Haq IU, Liu S, Jie W, Ali N, Shen W, Fang Y. A green catalytic pathway to sustainable poly(propylene carbonate) production: potassium phenyl thiolate/triethylboron-mediated copolymerization of CO_2 and propylene oxide. New J Chem. 2026; 50(4): 2023-31. https://doi.org/10.1039/D5NJ04492H

[3] Hu ZP, Yang D, Wang Z, Yuan ZY. State-of-the-art catalysts for direct dehydrogenation of propane to propylene. Chin J Catal. 2019; 40(9): 1233-54. https://doi.org/10.1016/S1872-2067(19)63360-7

[4] Chernyak SA, Corda M, Dath JP, Ordomsky VV, Khodakov AY. Light olefin synthesis from a diversity of renewable and fossil feedstocks: state of the art and outlook. Chem Soc Rev. 2022; 51(18): 7994-8044. https://doi.org/10.1039/D1CS01036K

[5] Bai PT, Manokaran V, Saiprasad PS, Srinath S. Studies on heat and mass transfer limitations in oxidative dehydrogenation of ethane over Cr_2O_3/Al_2O_3 catalyst. Procedia Eng. 2015; 127: 1338-45. https://doi.org/10.1016/j.proeng.2015.11.492

[6] Darvishi A, Davand R, Khorasheh F, Fattahi M. Modeling-based optimization of a fixed-bed industrial reactor for oxidative dehydrogenation of propane. Chin J Chem Eng. 2016; 24(5): 612-22. https://doi.org/10.1016/j.cjche.2015.12.018

[7] Gambo Y, Adamu S, Abdulrasheed AA, Lucky RA, Ba-Shammakh MS, Hossain MM. Catalyst design and tuning for oxidative dehydrogenation of propane: a review. Appl Catal A Gen. 2021; 609: 117914. https://doi.org/10.1016/j.apcata.2020.117914

[8] Skubic L, Sovdat J, Teran N, Hus M, Kopac D, Likozar B. Ab initio multiscale process modeling of ethane, propane and butane dehydrogenation reactions: a review. Catalysts. 2020; 10(12): 1405. https://doi.org/10.3390/catal10121405

[9] Liu SB, Zhang BF, Liu GZ. Metal-based catalysts for the non-oxidative dehydrogenation of light alkanes to light olefins. React Chem Eng. 2021; 6(1): 9-26. https://doi.org/10.1039/D0RE00381F

[10] Chen C, Hu ZP, Ren JT, Zhang SM, Wang Z, Yuan ZY. ZnO nanoclusters supported on dealuminated zeolite β as a novel catalyst for direct dehydrogenation of propane to propylene. ChemCatChem. 2019; 11(2): 868-77. https://doi.org/10.1002/cctc.201801708

[11] Jiang X, Sharma L, Fung V, Park SJ, Jones CW, Sumpter BG, *et al*. Oxidative dehydrogenation of propane to propylene with soft oxidants via heterogeneous catalysis. ACS Catal. 2021; 11(4): 2182-34. https://doi.org/10.1021/acscatal.0c03999

[12] Sun Z, Russell CK, Whitty KJ, Eddings EG, Dai JZ, Zhang YL, *et al*. Chemical looping-based energy transformation via lattice oxygen modulated selective oxidation. Prog Energy Combust Sci. 2023; 96: 101045. https://doi.org/10.1016/j.pecs.2022.101045

[13] Chen S, Pei CL, Chang X, Zhao ZJ, Mu RT, Xu YY, *et al*. Coverage-dependent behaviors of vanadium oxides for chemical looping oxidative dehydrogenation. Angew Chem Int Ed. 2020; 59(49): 22072-9. https://doi.org/10.1002/anie.202005968

[14] Wu TW, Yu QB, Roghair I, Wang K, van Sint Annaland M. Chemical looping oxidative dehydrogenation of propane: a comparative study of Ga-based, Mo-based, V-based oxygen carriers. Chem Eng Process Process Intensif. 2020; 157: 108137. https://doi.org/10.1016/j.cep.2020.108137

[15] Wu TW, Yu QB, Qin Q. Energy analysis of chemical looping oxidative dehydrogenation of propane. Pet Sci Technol. 2018; 36(4): 266-72. https://doi.org/10.1080/10916466.2017.1416631

[16] Sun Z, Cai TY, Russell CK, Johnson JK, Ye RP, Xiang WG, *et al*. Highly efficient methane decomposition to H_2 and CO_2 reduction to CO via redox looping of $Ca_2Fe_xAl_{2-x}O_5$-supported $Ni_\gamma Fe_{3-\gamma}O_4$ nanoparticles. Appl Catal B Environ. 2020; 271: 118938. https://doi.org/10.1016/j.apcatb.2020.118938

[17] Qiang FY, Guo T, Nie MD, Liu YZ, Wu M, Guo QJ. Effect of Ce content on the chemical looping oxidative dehydrogenation of propane to propylene over a VO_x-CeO_2/γ-Al_2O_3 oxygen carrier. Catalysts. 2023; 13(5): 797. https://doi.org/10.3390/catal13050797

[18] Chen DK, Zhang DH, He DD, Lu JC, Zhong LP, Han CY, *et al*. Relationship between oxygen species and activity/stability in heteroatom (Zr, Y)-doped cerium-based catalysts for catalytic decomposition of CH_3SH. Chin J Catal. 2018; 39(12): 1929-41. https://doi.org/10.1016/S1872-2067(18)63146-8

[19] Bu CS, Gu TT, Cen ST, Liu DY, Meng JG, Liu CQ, *et al*. Reactivity and stability of Zr-doped CeO_2 for solar thermochemical H_2O splitting in combination with partial oxidation of methane via isothermal cycles. Int J Hydrogen Energy. 2023; 48(33): 12227-39. https://doi.org/10.1016/j.ijhydene.2022.11.232

[20] Hong S, Seo BH, Bae JW. Chemical looping-based oxidative dehydrogenation of ethane and successive CO_2 activation on Fe-modified $CeZrO_x$ mixed-metal oxides. Energy Fuels. 2025; 39(30): 14752-64. https://doi.org/10.1021/acs.energyfuels.5c00947

[21] Xie QH, Zhang HM, Kang JC, Cheng J, Zhang QH, Wang Y. Oxidative dehydrogenation of propane to propylene in the presence of HCl catalyzed by CeO_2 and NiO-modified CeO_2 nanocrystals. ACS Catal. 2018; 8(6): 4902-16. https://doi.org/10.1021/acscatal.8b00650

[22] Zhang LJ, Chen RH, Tu Y, Gong XY, Cao X, Xu Q, *et al*. Revealing the crystal facet effect of ceria in Pd/CeO_2 catalysts toward the selective oxidation of benzyl alcohol. ACS Catal. 2023; 13(4): 2202-13. https://doi.org/10.1021/acscatal.2c04252

[23] Zhou GL, Li T, Chen JY, Deng LD, Xie HM. Nano-Pd/CeO_2 catalysts for hydrogen storage by reversible benzene hydrogenation/dehydrogenation reactions. Int J Hydrogen Energy. 2021; 46(27): 14540-55. https://doi.org/10.1016/j.ijhydene.2021.01.235

[24] Hosono Y, Saito H, Higo T, Watanabe K, Ito K, Tsuneki H, *et al*. Co-CeO_2 interaction induces the Mars-van Krevelen mechanism in dehydrogenation of ethane. J Phys Chem C. 2021; 125(21): 11411-8. https://doi.org/10.1021/acs.jpcc.1c02855

[25] Zhang ZQ, Ding J, Chai RJ, Zhao GF, Liu Y, Lu Y. Oxidative dehydrogenation of ethane to ethylene: a promising CeO_2-ZrO_2-modified NiO-Al_2O_3/Ni-foam catalyst. Appl Catal A Gen. 2018; 550: 151-9. https://doi.org/10.1016/j.apcata.2017.11.005

[26] Su Y, Yang WY, Sun WZ, Li Q, Shang JK. Synthesis of mesoporous cerium-zirconium binary oxide nanoadsorbents by a solvothermal process and their effective adsorption of phosphate from water. Chem Eng J. 2015; 268: 270-9. https://doi.org/10.1016/j.cej.2015.01.070

[27] Zuo C, Wu M, Guo QJ. The effect of the Ce content on the oxidative dehydrogenation of propane over CrO_γ-CeO_2/γ-Al_2O_3 catalysts. Chin J Chem Eng. 2020; 28(12): 3035-43. https://doi.org/10.1016/j.cjche.2020.04.022

[28] Campos PTA, Oliveira CF, Lima JPV, Silva DRD, Dias SCL, Dias JA. Cerium-zirconium mixed oxide synthesized by sol-gel method and its effect on the oxygen vacancy and specific surface area. J Solid State Chem. 2022; 307: 122752. https://doi.org/10.1016/j.jssc.2021.122752

[29] Turakulova AO, Kharlanov AN, Levanov AV, Isaikina OY, Lunin VV. Catalytic properties of the $VO_x/Ce_{0.46}Zr_{0.54}O_2$ oxide system in the oxidative dehydrogenation of propane. Russ J Phys Chem A. 2017; 91(1): 17-25. https://doi.org/10.1134/S0036024417010307

[30] Daniel C, Schuurman Y, Farrusseng D. Surface effect of nano-sized cerium-zirconium oxides for the catalytic conversion of methanol and CO_2 into dimethyl carbonate. J Catal. 2021; 394: 486-94. https://doi.org/10.1016/j.jcat.2020.09.023

[31] Vu BK, Shin EW, Ha JM, Kim SK, Suh DJ, Kim WI, *et al*. The roles of $Ce_\gamma Zr_{1-\gamma}O_2$ in propane dehydrogenation: enhancing catalytic stability and decreasing coke combustion temperature. Appl Catal A Gen. 2012; 443-444: 59-66. https://doi.org/10.1016/j.apcata.2012.07.022

[32] Oliveira CF, Garcia FAC, Araújo DR, Macedo JL, Dias SCL, Dias JA. Effects of preparation and structure of cerium-zirconium mixed oxides on diesel soot catalytic combustion. Appl Catal A Gen. 2012; 413-414: 292-300. https://doi.org/10.1016/j.apcata.2011.11.020

[33] Deng J, Li SS, Xiong L, Wang JL, Yuan SD, Chen YQ. Different thermal behavior of nanostructured CeO_2-ZrO_2-based oxides with varied Ce/Zr molar ratios. Mater Chem Phys. 2019; 236: 121767. https://doi.org/10.1016/j.matchemphys.2019.121767

[34] King A, Singh R, Anand R, Behera SK, Nayak BB. Spectroscopic studies of borohydride-derived cerium-doped zirconia nanoparticles under air and argon annealing conditions. J Nanopart Res. 2021; 23(8): 156. https://doi.org/10.1007/s11051-021-05299-x

[35] Shah PM, Burnett JWH, Morgan DJ, Davies TE, Taylor SH. Ceria-zirconia mixed metal oxides prepared via mechanochemical grinding of carbonates for the total oxidation of propane and naphthalene. Catalysts. 2019; 9(5): 475. https://doi.org/10.3390/catal9050475

[36] Wu YL, Zhao WJ, Li XH, Li WY. Effects of Al doping on CeZr solid solution for oxidative dehydrogenation of ethylbenzene with CO_2. J Fuel Chem Technol. 2017; 45(2): 189-93. https://doi.org/10.1016/S1872-5813(17)30014-2

[37] Kaminski P, Ziolek M, van Bokhoven JA. Mesoporous cerium-zirconium oxides modified with gold and copper: synthesis, characterization and performance in selective oxidation of glycerol. RSC Adv. 2017; 7(13): 7801-19. https://doi.org/10.1039/C6RA27671G

[38] Han SL, Zhao D, Otroshchenko T, Lund H, Bentrup U, Kondratenko VA, *et al*. Elucidating the nature of active sites and fundamentals for their creation in Zn-containing ZrO_2-based catalysts for nonoxidative propane dehydrogenation. ACS Catal. 2020; 10(15): 8933-49. https://doi.org/10.1021/acscatal.0c01580

[39] Daniel S, Monguen CKF, El Kasmi A, Arshad MF, Tian ZY. Oxidative dehydrogenation of propane to olefins promoted by Zr-modified ZSM-5. Catal Lett. 2023; 153(1): 285-99. https://doi.org/10.1007/s10562-022-03977-6

[40] Linstrom PJ, Mallard WG, editors. NIST Chemistry WebBook, NIST Standard Reference Database Number 69. Gaithersburg (MD): National Institute of Standards and Technology. Available from: https://webbook.nist.gov/chemistry/ (Accessed on 19 July, 2026).

[41] Cavani F, Ballarini N, Cericola A. Oxidative dehydrogenation of ethane and propane: how far from commercial implementation? Catal Today. 2007; 127(1-4): 113-31. https://doi.org/10.1016/j.cattod.2007.05.009

[42] Zeng L, Cheng Z, Fan JA, Fan LS, Gong J. Metal oxide redox chemistry for chemical looping processes. Nat Rev Chem. 2018; 2(11): 349-64. https://doi.org/10.1038/s41570-018-0046-2

[43] Zhu X, Imtiaz Q, Donat F, Müller CR, Li F. Chemical looping beyond combustion: a perspective. Energy Environ Sci. 2020; 13(3): 772-804. https://doi.org/10.1039/C9EE03793D

[44] Gao Y, Haeri F, He F, Li F. Alkali metal-promoted $La_xSr_{2-x}FeO_{4-\delta}$ redox catalysts for chemical looping oxidative dehydrogenation of ethane. ACS Catal. 2018; 8(3): 1757-66. https://doi.org/10.1021/acscatal.7b03928

[45] Yusuf S, Neal L, Bao Z, Wu Z, Li F. Effects of sodium and tungsten promoters on Mg_6MnO_8-based core-shell redox catalysts for chemical looping oxidative dehydrogenation. ACS Catal. 2019; 9(4): 3174-86. https://doi.org/10.1021/acscatal.9b00164

[46] Chen S, Zeng L, Mu R, Xiong C, Zhao ZJ, Peng L, *et al*. Modulating lattice oxygen in dual-functional Mo-V-O mixed oxides for chemical looping oxidative dehydrogenation. J Am Chem Soc. 2019; 141(47): 18653-57. https://doi.org/10.1021/jacs.9b09235

[47] Wang C, Yang B, Gu Q, Han Y, Tian M, Su Y, *et al*. Near 100% ethene selectivity achieved by tailoring dual active sites in chemical looping oxidative dehydrogenation. Nat Commun. 2021; 12: 5447. https://doi.org/10.1038/s41467-021-25782-2

[48] Chen X, Tian X, Zheng C, Zhao H. $CrO_x/Ce_{1-x}Zr_xO_2$ for chemical looping oxidative dehydrogenation of propane. Chem Eng Sci. 2023; 274: 118697. https://doi.org/10.1016/j.ces.2023.118697

[49] Wang X, Pei C, Zhao ZJ, Chen S, Li X, Sun J, *et al*. Coupling acid catalysis and selective oxidation over MoO_3-Fe_2O_3 for chemical looping oxidative dehydrogenation of propane. Nat Commun. 2023; 14: 2039. https://doi.org/10.1038/s41467-023-37818-w

[50] Oing A, Donat F, Müller CR. Controlling selectivity in chemical looping oxidative dehydrogenation of propane through interface engineering. Nat Commun. 2025; 16: 5247. https://doi.org/10.1038/s41467-025-60428-7

Supplementary Table

Table S1: Strength of (111), (200), (220), (311) crystal planes of CeO_2 and $CeZrO_X$ mixed metal oxide carriers

Oxygen Carrier	111	200	220	311
CeO_2	1321	514	648	493
$Ce_{0.95}Zr_{0.05}O_x$	1402	534	693	512
$Ce_{0.90}Zr_{0.10}O_x$	1882	578	728	530
$Ce_{0.75}Zr_{0.25}O_x$	1576	545	658	509
$Ce_{0.50}Zr_{0.50}O_x$	1145	503	597	486